International Journal of Hydrogen Energy 175 (2025) 151347

Contents lists available at ScienceDirect

International Journal of Hydrogen Energy

journal homepage: www.elsevier.com/locate/he

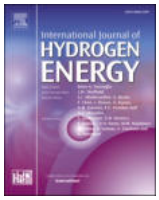

Hydrogen and ICEs: validation of a 3D-CFD approach for in-cylinder combustion simulations of ultra-lean mixtures with a focus on the combustion regime

Stefano Sfriso [a,*], Fabio Berni [a], Caio Ramalho Leite [b], Sebastiano Breda [a], Fabriche Foucher [b], Pierre Brequigny [b], Jacques Borée [c], Stefano Fontanesi [a]

[a] Università Degli Studi di Modena e Reggio Emilia, Italy
[b] University of Orléans, France
[c] ISAE-ENSMA, France

ARTICLE INFO

Handling editor: A.B. Basile

ABSTRACT

This paper proposes a numerical setup for 3D-CFD in-cylinder simulations of H_2-fuelled internal combustion engines. The flamelet G-equation model, based on Verhelst and Damköhler-like correlations for laminar and turbulent flame speeds respectively, is used to reproduce the flame propagation. The validation against experimental data from a homogeneous-mixture port-injection engine enables a focus on combustion simulation by minimising stratification uncertainties. Accurate flame propagation modelling is identified as the main challenge. The results on different operating conditions confirm the predictive capabilities of the framework, thanks to the agreement with the experimental pressure traces, combustion indicators and flame imaging. Notably, combustion rate predictions remain accurate even without considering the flame thermo-diffusive instability, as the turbulence effect dominates at the investigated conditions. The combustion regime is analysed by a modified Borghi-Peters diagram and it ranges from flamelet to thin reaction zones. This highlights the numerical setup flexibility, which accurately simulates combustion across different regimes.

1. Introduction

In the last years, the growing attention on renewable sources, pollution and greenhouse gas emissions has boosted research on green hydrogen for automotive applications. H_2 intended as e-fuel is potentially renewable, as it can be produced by electrolysis, starting from water and electric energy obtained via renewable sources (such as wind and solar energies). As for the air pollution, H_2 can be exploited in fuel cells which are characterised by zero emissions. Alternatively, it can be used to fuel internal combustion engines (ICEs) and, in this case, apart from traces of unburnt hydrocarbons and particulate matter due to combustion of the lubricating oil present in the cylinder, only NO_x emissions can be noticed at the exhaust [1]. Therefore, even for ICEs, the use of H_2 is beneficial for the reduction of pollutants. Moreover, for both fuel cells and ICEs, adopting green H_2 leads to zero CO_2 emissions and, thus, to carbon neutrality. Finally, from a technological standpoint, the role of H_2 and in general of e-fuels is of primary importance, as they can ensure the survival of consolidated solutions such as the internal combustion engine. A recent EU regulation [2] has straightened, for passenger cars and light commercial vehicles, the CO_2 emission standards. Starting from 2035, new means of transport of such categories will have to be characterised by zero greenhouse gas emissions. This represents, de facto, a ban on ICEs fuelled with traditional fuels. However, ICEs supplied with CO_2-neutral fuels could still be employed. For example, as previously discussed, green H_2 does not lead to CO_2 emissions at the exhaust. Moreover, also e-gasoline or biofuels (such as biodiesel) may be adopted. Although they are characterised by CO_2 emissions, they are carbon neutral as the CO_2 emitted during combustion corresponds to the one previously adsorbed during production. In particular, the e-gasoline formation relies on CO coming from CO_2 adsorbed in the atmosphere. As for biofuels, they are produced by biomass that adsorbed CO_2 during its life [3]. Therefore, even if ICEs fuelled with e-gasoline or biofuels are not formally zero greenhouse gas emission solutions, they are carbon neutral anyway. Not by chance, in Ref. [2], there is a paragraph dedicated to CO_2-neutral fuels, which leaves a possibility for a future opening of the European Union to ICEs

* Corresponding author.
E-mail address: stefano.sfriso@unimore.it (S. Sfriso).

https://doi.org/10.1016/j.ijhydene.2025.151347
Received 22 April 2025; Received in revised form 27 August 2025; Accepted 2 September 2025
Available online 13 September 2025

supplied with such fuels.

The research on H_2 ICEs is not a novelty. In literature, several papers can be found, dealing with both experimental and numerical activities. For brevity, only the most relevant and recent research activities are reviewed in the following and, on the numerical side, the attention is focused on CFD works.

Focusing on the experimental side, several concepts or aspects are investigated by the research community. For instance, Luo et al. [4] and Marwaha et al. [5] experimentally study NO_x emissions at different operating conditions, while in other works the attention is focused on the balance between thermal efficiency and waste energy recovery from the turbocharger in boosted hydrogen engines [6]. Tsujimura and Suzuki [7] develop a stationary hydrogen engine with large displacement. Leite et al. [8,9] analyse combustion of ultra-lean H_2 engines, focusing on the description of the combustion initiation. Fontanesi et al. [10] and Postrioti et al. [11] carry out experimental characterisations of hydrogen jets along with 3D-CFD analyses to deepen the involved phenomena.

Similarly, the numerical works aim to highlight the potential of CFD to develop H_2 ICEs. Among the possible tasks, CFD is often adopted to optimise the combustion process (in place of expensive experiments), increasing efficiency and simultaneously reducing NO_x emissions. However, in order to exploit the potential of CFD for the simulation of H_2 ICEs, new models have to be developed or the existing ones (well-consolidated for traditional fossil fuels) need ad-hoc validation.

As for the development of new models, ultra-lean hydrogen combustion poses novel challenges due to the inherent complexities of H_2 flames. Probably, the most relevant peculiarity of hydrogen combustion is represented by thermo-diffusive (TD) instabilities. Therefore, a modelling approach able to include their effect is of primary importance. In this regard, recent studies try to deepen the role of TD instabilities in H_2 flames, such as the ones proposed by Berger et al. [12–14] and Howarth et. at. [15,16]. In these studies, hydrogen flames are simulated in a small domain by means of direct numerical simulations (DNS) carried out at pressure and temperature typical of internal combustion engines operations. Laminar simulations are carried out in both 2D and 3D domains, observing differences in the hydrogen unstretched laminar flame speed enhancement due to the possibility for TD instabilities to manifest in 2 or 3 directions. Moreover, in both Berger and Howarth works, 3D turbulent simulations are also performed to investigate the mutual interaction between turbulence and instabilities. However, the investigated operating conditions are limited compared to the possible combinations of chemistry and turbulence conditions that can be experienced in ICEs. Other works such as the experimental ones of Bradley et al. [17,18] try to clarify the actual effect of the TD instabilities in turbulent flows. Although the literature has yet to reach a definitive conclusion on this topic, some key aspects can be inferred. Notably, the accelerating effect of the TD instabilities in laminar flows of lean H_2-air mixtures is well established. In addition, such effect depends in a complex way on pressure, temperature and equivalence ratio. In case of mild turbulence, the overall flame propagation speed is governed by both turbulence and instabilities. For high turbulence levels, the flame acceleration is primarily driven by turbulence itself rather than TD instability effects. However, aspects such as the time required for the instability to fully develop remain scarcely explored. This is important considering that, on the one hand, most of the conclusions from the DNS are based on statistically steady flames and, on the other hand, combustion is highly unsteady and rapid in ICEs, meaning that the steady-state findings may not directly apply to real engine conditions. Concluding, modelling and relevance of TD instabilities still represent an open debate in the context of H_2 ICEs.

In literature, the efforts of the authors are not only focused on the proposal of new models, but also on their validation. Different numerical approaches to H_2 combustion simulation are tested in previous works. Detailed Chemistry (DC) is widely diffused. For instance, SAGE model is employed by Liu et al. [19] to model H_2 combustion with turbulent jet ignition (TJI) and by Babayev et al. [20] to investigate a compression ignition H_2 engine. Other authors prefer the adoption of flamelet models. Gerke et al. [21] rely on the laminar flame concept of Peters [22] along with a turbulent flame closure to describe the global reaction progress. The main critical aspect in Ref. [21] is that it is not possible to define a unique set of calibration parameters of the combustion model able to provide reliable results for all the investigated conditions. Different works rely on the Coherent Flame Model (CFM) or its "Extended" version (ECFM). In particular, Pielecha et al. [23] exploit the CFM for a numerical study on a TJI hydrogen engine, so no validation is presented. Rouleau et al. [24] adopt the ECFM to investigate a high-compression-ratio direct-injection hydrogen engine. Maio et al. [25] compare 3D-CFD results obtained by ECFM model with experimental data on a hydrogen engine equipped with both port fuel injection (PFI) and direct injection (DI) systems. Knop et al. [26] investigate two hydrogen engines, one PFI characterised by a cryogenic injection system, and one DI, using ECFM. However, these works based on CFM or ECFM are characterised by a scarce validation against experiments (i.e. few operating conditions are considered for comparison). Moreover, the two combustion models often undergo a case-by-case calibration, as a confirmation of the poor predictive capabilities of the selected numerical frameworks. In literature, there are also works relying on combinations of "flamelet" models and DC. Hernandez et al. [27] simulate ultra-lean hydrogen combustion using G-equation model paired with tabulated chemistry for the laminar flame speed computation, also considering thermo-diffusive instabilities. Sfriso et al. [28] and Berni et al. [29] adopt G-equation coupled with DC for the online calculation of the burnt gas composition. Therefore, the heat release rate is governed by both G-Equation and DC.

In conclusion, none of the above-mentioned works is characterised by extended validation on a wide set of operating points with single calibration of the models. For this reason, the present paper aims to propose and extensively validate a 3D-CFD approach for in-cylinder analyses of H_2 ICEs. The validation is carried out on 15 operating conditions (including ultra-lean ones) by using a unique set of model calibration constants. The numerical approach exploits the G-equation combustion model fed by a Damköhler-like correlation of turbulent flame speed [30–32] in which the laminar flame speed is provided by Verhelst correlation [33]. The experimental activity is performed on an optical research engine derived from the gasoline PSA EP6.

The validation of the numerical approach proposed in the present paper starts from previous works by the authors [34,35], where it is shown to be effective in predicting the performance of a Diesel engine converted to H_2. The investigated powertrain is direct injection and the numerical analyses are performed on a set of 11 cases, characterised by different values of equivalence ratio and revving speed. However, in order to focus better the validation on the combustion process, the authors also investigate a PFI engine in Ref. [35]. This power unit is the same PSA EP6 analysed in the present paper, in which the port injection strategy ensures homogeneous mixture in the combustion chamber. Compared to Ref. [35], where few conditions are investigated, in this work the validation process is stressed. In fact, 15 operating points are considered, characterised by different revving speeds, spark timings, indicated mean effective pressure (IMEP) values, and equivalence ratios (from 0.30 to 0.55). Interestingly, the calibration parameters of the models are the same for all the 15 cases and also corresponding to those adopted for the simulations of the Diesel-derived H_2 engine investigated in Refs. [34,36]. In addition, for all the analysed conditions, the thermo-diffusive instability is neglected as the effect is deemed to be minimal. Finally, still in comparison with [35], an insight into the combustion regime is proposed. In fact, because of the wide set of operating points, multiple combustion regimes characterise the engine operation [9] and, nevertheless, the adopted "flamelet" combustion model is able to work properly for all the conditions.

The proven predictive capabilities of the proposed numerical approach open the possibility to its use for future design exploration and

engine calibration analyses. This is crucial as a robust numerical 3D-CFD methodology allows engineers to virtually address the challenges related to H_2 ICEs with lower cost and time-to-market compared to experiments.

After the introduction, the experimental apparatus along with the engine are described. Numerical setup details are then deepened. Afterward, the CFD outcomes are compared to the experimental ones. Finally, before the conclusions, a discussion of the simulation results in connection with the identified combustion regimes is proposed.

2. Investigated engine and experimental apparatus

A four-valve spark-ignition single-cylinder optical engine is investigated, whose specifications are reported in Ref. [35]. The engine is characterised by tumble-promoting intake ports and a piston with optical access. Nonetheless, the piston shape is similar to the original gasoline engine. The bowl features a quartz window allowing for hydrogen flame visualization by a high-speed camera (Phantom v1610) exploiting the chemiluminescence. It is characterised by band-pass filter (with a centre wavelength of 318 nm and a full width at half-maximum of 175 nm) and high-speed Intensified Relay Optics (LaVision HS IRO). Image acquisition occurs at a frequency of 1 image/° CA, with a magnification ratio of 0.092 mm/pixel. Camera exposure time and gain of the intensifier vary based on the equivalence ratio (φ) and, by varying φ between 0.55 and 0.30, they range from 30 μs and 50 % to 80 μs and 65 %. As for the ignition, the three-mass-electrodes Bosch ZLR07MTE spark plug is chosen. It is preferred with hydrogen as it represents a valid compromise between cycle-to-cycle variability minimization at low loads and knock tendency reduction at high loads. Fig. 1 shows a model of the additional ducts and plenums placed at intake and exhaust. Interestingly, in order to ensure mixture homogeneity, hydrogen is introduced by a 6 mm pipe located near the intake plenum (in correspondence of the blue manifold), i.e. far from the intake valves. Moreover, the duct length is chosen to let the turbulent macro structures generating at the junction with plenum dissipate. For further information, the experimental setup is detailed in Ref. [8].

In Fig. 2, a block diagram of the test bench is reported. As visible, sensors record, with a 0.01 °CA resolution, the pressure in the intake and exhaust plenums and in the cylinder. The cycle-resolved pressure values are averaged on 100 consecutive cycles and adopted in the simulations as boundary conditions and for validation, respectively. The adopted piezoelectric pressure sensor is an AVL QH32C quartz transducer characterised by a range of 200 bar and a sensitivity of 26.82 pC/bar, with a maximum linearity error of ±0.25 % of the full-scale output. In order to control the mixture quality, the mass flow rates of the aspirated air and injected hydrogen are measured. The temperatures of the exhaust and intake plenums are also measured. Because of the intrinsic thermal inertia of the thermocouples, the time resolution is poor and it is not possible to obtain cycle-resolved traces. As a consequence, constant temperature values are adopted as boundary conditions for the simulations.

The tested operating conditions are resumed in Table 1. The cases 1 to 6 are characterised by the same spark time, intake pressure and engine speed, while the equivalence ratio varies from 0.30 to 0.55. The cases 7 to 10 have the same spark advance of the previous ones while the intake pressure is fixed to 0.9 bar. The equivalence ratio sweeps from 0.30 to 0.45. Finally, the conditions of the cases 11 to 15 are obtained by pursuing the same IMEP. This is obtained by increasing φ and reducing spark advance and intake pressure. For these cases, the engine speed lowers from 1500 to 1200 rpm.

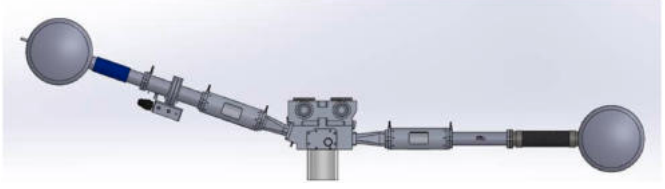

Fig. 1. Model showing the engine head (along with the cylinder) as well as intake (on the left) and exhaust (on the right) ducts and plenums.

3. 3D-CFD model setup

The adopted CFD tool is the commercial code STAR-CD, licensed by SIEMENS DISW and extensively adopted by the authors in the past. An Unsteady Reynolds Average Navier Stokes (URANS) approach is preferred, exploiting the k-ε RNG model [37,38] for the turbulence closure. This model is widely used in literature and by the authors in many publications [39–44]. The near-wall flow is modelled by a high-Reynolds wall treatment to minimize the computational time. The "Improved GruMo-UniMORE" model is used for the heat transfer prediction [45–47]. It is independent of the near-wall grid resolution and it uses the effective Prandtl number of the gas mixture. The time-step is equal to 0.05° crank angle (CA) during ignition, combustion and valve motion. During the rest of the cycle, it is set to 0.1° CA. The 0° CA corresponds to the Top Dead Centre of firing (TDCf) and the simulation starts during the expansion stroke, i.e. at 90° CA. The first cycle is initialized with guessed fields of temperature, pressure and velocity and then, multiple cycles are run for each operating point in order to reduce the sensitivity to the initial conditions. Three cycles are sufficient to reach a cycle to cycle convergence of the pressure traces.

According to the experimental test specifically prepared to ensure homogeneity, a perfectly premixed hydrogen-air mixture is imposed at the inlet boundary of the model. As anticipated in the previous paragraph, experimentally derived time-dependent conditions of pressure are applied at the intake and exhaust boundaries. In this regard, Fig. 3 shows an example of pressure boundary conditions. As for the temperature, constant values are imposed, and they are reported in Table 1.

As for the solid boundaries, a dedicated temperature is specified for each single wall, based on the author's experience on heat transfer analysis [48–50]. More details can be found in Ref. [35].

The ignition is treated by an in-house developed approach based on a sub-grid model. The latter has been extensively validated within a large eddy simulation (LES) framework [51,52] and, for the present study, a URANS version is used. In the current implementation, the delay related to the electric circuit is neglected. The reason is the time interval between nominal spark time and actual breakdown, which is approximately 10 μs and, thus, negligible at the investigated engine speeds [53–55].

The model starts with the deposition of an initial spherical flame kernel. Then, its growth is governed by a 1D ordinary differential equation (ODE) whose unknown is the kernel radius. The equation is solved starting from the spark timing until a threshold value for the unknown variable is reached. The 1D ODE is detailed in Equation (1) and it is similar to the Herweg and Maly model [56].

$$\frac{dr_k}{dt} = \frac{\rho_u}{\rho_k}(S_l + S_{Plasma}) + \frac{V_k}{A_k}\left[\frac{1}{T_k}\frac{dT_k}{dt}\right] \tag{1}$$

In Equation (1), r_k, ρ_k, T_k, V_k and A_k are kernel-related quantities and they are radius, density, temperature, volume and surface area, respectively. The other quantities are time t, density of the unburned gases ρ_u, laminar flame speed S_l and expansion velocity of the plasma column forming in the spark gap S_{Plasma}. Unlike Herweg and Maly model, the present approach relies on a laminar flame speed inside Equation (1), instead of a turbulent one. Once a threshold value of r_k is reached, the ignition model (i.e. the ODE) stops and the flame propagation is governed by G-equation. As for the threshold value, 2.3 mm is adopted. This is coherent with [56], where the turbulence contribution is suggested to be significant after ≈ 2 mm, thus reducing the accuracy of the 1D model.

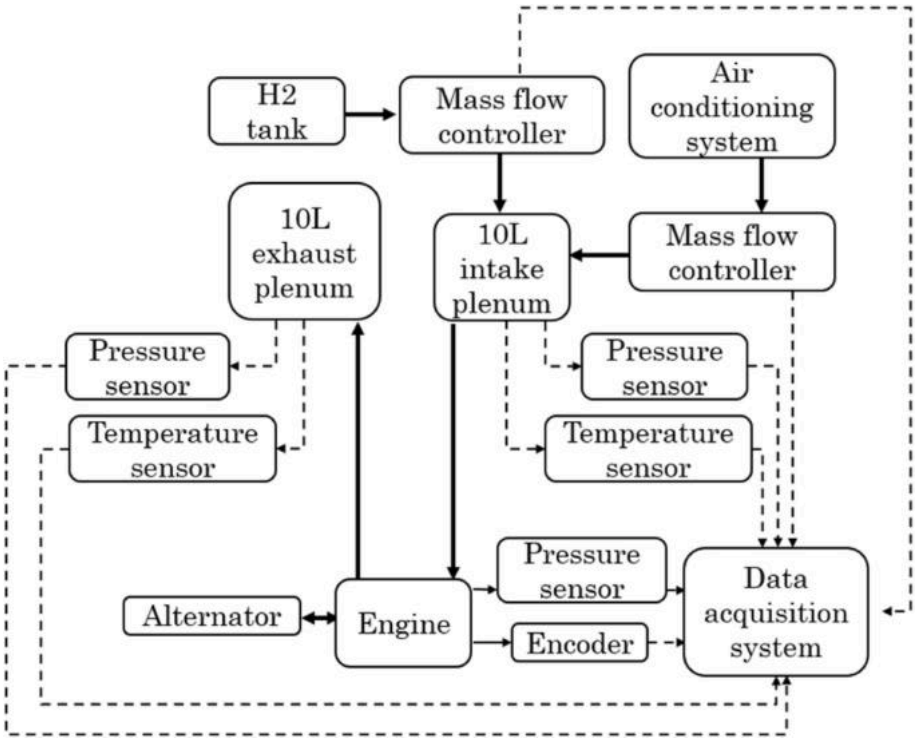

Fig. 2. Test bench block diagram.

Table 1
Operating points investigated at the bench and utilized for simulation validation. bTDC and CoV stand for before Top Dead Centre and Coefficient of Variation.

Case Number #	φ	Ignition [° CA bTDC]	Intake temperature [K]	Exhaust temperature [K]	Average intake pressure [bar]	rpm	CoV IMEP [%]
1	0.30	15	295.7	596.0	0.70	1500	4.87
2	0.35	15	295.7	608.6	0.70	1500	2.14
3	0.40	15	295.8	623.7	0.70	1500	1.37
4	0.45	15	295.9	635.0	0.70	1500	0.97
5	0.50	15	296.0	658.4	0.70	1500	1.17
6	0.55	15	296.0	666.2	0.70	1500	1.51
7	0.30	15	295.2	590.4	0.90	1500	3.66
8	0.35	15	295.3	598.8	0.90	1500	1.81
9	0.40	15	295.5	612.6	0.90	1500	1.45
10	0.45	15	295.7	623.0	0.90	1500	1.10
11	0.35	23	296.2	544.0	0.89	1200	1.42
12	0.40	18	296.5	566.6	0.82	1200	1.07
13	0.45	14	296.7	599.2	0.75	1200	1.37
14	0.50	11	296.9	597.2	0.73	1200	1.20
15	0.55	8	297.0	610.0	0.72	1200	1.13

In order to infer the value of S_{Plasma}, Equation (2) is employed, which is a one-dimensional unsteady heat conduction equation.

$$\rho c_p \frac{\partial T}{\partial t} = \frac{\partial}{\partial x}\left(k \frac{\partial T}{\partial x}\right) \tag{2}$$

The quantities appearing in Equation (2) are density ρ, specific heat c_p, temperature T, time t, space (radial) coordinate x and thermal conductivity k. As all these properties are related to plasma, the experimental measure is difficult. Estimations can be found in Refs. [57–63], where the product ρc_p is proposed equal to 8000 J/(m^{3}K), while thermal conductivity and boundary condition for Equation (2), i.e. the temperature at $x = 0$, are suggested equal to 0.2 W/(mK) and $60 \cdot 10^3$ K, respectively.

The initial condition of Equation (1), namely the initial value of r_k ($r_{k,init}$), is evaluated via a simplified method similar to the one proposed by Colin [64]. The initial kernel is assumed as a perfect sphere with radius $r_{k,init}$, whose volume equals the volume of the plasma channel formed between the electrodes, supposed as a perfect cylinder. In this regard, the height of the cylinder corresponds to the spark gap (d_{gap} = 0.5 mm in this case) while the radius is the laminar flame thickness (δ_l) at the unburnt gas conditions at the spark-plug. Equation (3) expresses the volume of the cylinder, from which $r_{k,init}$ can be inferred, as shown by Equation (4).

$$V_{k,init} = d_{gap} \pi \delta_l^{\,2} \tag{3}$$

$$r_{k,init} = \left(\frac{3}{4\pi} V_{k,init}\right)^{1/3} \tag{4}$$

It is worth noting that the adoption of Equation (3) is related to the fact that, if the ignition is successful, the volume of the initial kernel is assumed for simplicity equal to the plasma channel one. The latter is modelled as a cylinder characterised by a height equal to the spark gap

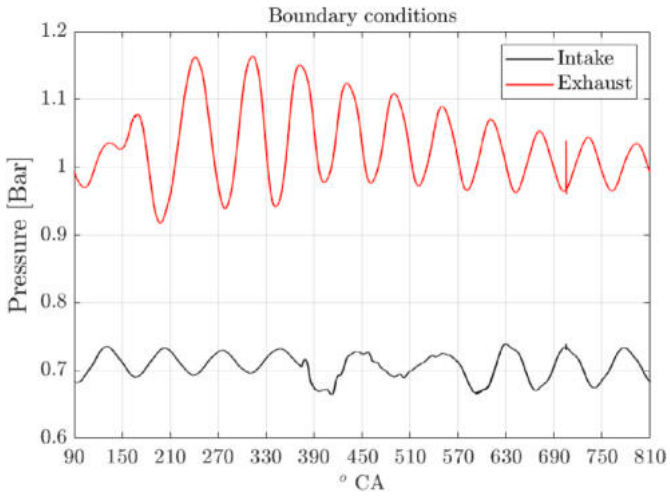

Fig. 3. Intake and exhaust time-dependent pressure boundary conditions for case #6.

and a radius equal to the laminar flame thickness [65]. The spark gap is selected as the spark extends between the electrodes. As for the laminar flame thickness, its adoption ensures that the kernel radius is fixed at the minimum. In fact, once the cylindrical geometry is assumed for the kernel, the radius cannot be lower than the laminar flame thickness. For each operating point, the value of δ_l is calculated using 1D steady-state simulations of freely propagating flame in DARS v2020.1, licensed by SIEMENS DISW. The governing equations are detailed in the DARS user guide [66]. The simulations employ the chemical kinetics mechanism proposed by Konnov [67]. The thermodynamic conditions found at the spark plug in the 3D-CFD simulations are used for the 1D computations and they are resumed in Table 2. The last two columns of the same table report the computed laminar flame thickness and the corresponding flame kernel dimension, for all the tested operating conditions.

As previously anticipated, G-equation is used to model the turbulent premixed combustion. The model uses a level-set method that tracks the scalar G representing the distance from the flame front by the transport equation reported in Equation (5). The iso-surface where G = 0 indicates the flame front position, while positive values of this scalar conventionally fall in the burnt region.

$$\frac{\partial}{\partial t}\rho G + \frac{\partial}{\partial x_i}\rho u_i G = \rho S_t |\nabla G| \tag{5}$$

In order to mimic the structure of a turbulent flame, the variance of G is considered, which is utilized to compute the turbulent flame thickness. The latter is necessary to represent the evolution of the combustion reactions across the flame front. In this regard, a regress variable (c) is calculated based on the brush thickness. For further details, it is possible to refer to Ref. [68]. In Equation (5), t is the time, x_i is the position in the i-direction, u_i is the velocity in the i-direction and ρ is the density. The turbulent flame speed S_t is computed by a Damköhler-like empirical relation reported in Equation (6) [69].

$$S_t = S_l\left(1 + A \cdot \left(\frac{u'}{S_l}\right)^{\frac{5}{6}}\right) \tag{6}$$

S_l and u' represent the laminar flame speed and the rms of the turbulent velocity fluctuations. u' is computed in the simulations as $\sqrt{\frac{2}{3}tke}$, where tke is the turbulent kinetic energy. The empirical coefficient A is set to 3.3 in this study. The laminar flame speed is calculated using Verhelst correlation [33], which fits chemical kinetics computation results obtained with Konnov mechanism [67]. This correlation is valid for the following ranges of pressure (p), temperature (T), equivalence ratio (φ), and exhaust gases recirculation (EGR): 5 bar ≤ p ≤ 45 bar, 500 K ≤ T ≤ 900 K, 0.33 ≤ φ ≤ 5, and 0 % ≤ EGR ≤50 %. The combinations of pressure, unburnt temperature and equivalence ratio experienced by the mixture throughout the cases are various but always inside the validation ranges of Verhelst correlation (except for the two conditions at φ = 0.30 which are, however, really close to the lower limit of 0.33). This correlation does not account for the flame acceleration due to thermo-diffusive instabilities, which are not considered in the present paper. The reason for this approximation can be found in Ref. [35]. In Ref. [35], the works of Matalon [70] and Howarth [16] are recalled. Matalon models the perturbation of a finite-thickness planar flame as a wave, whose growth rate (ω) is computed by a second-order expression. In Ref. [16], the second order component (ω_2) of the flame instability growth rate is used by Howarth et al. to correlate the unstretched laminar flame speed and the one accelerated by the thermo-diffusive instabilities as measured from 3D DNS. Howarth shows that, the higher ω_2 is, the higher the contribution of the TD instability becomes. ω_2, representing the TD contribution, is shown in Ref. [35] for some of the operating points investigated in the present paper, to prove that thermo-diffusive instabilities have limited influence on engine performance prediction. More in detail, in Ref. [35] it is shown that, for the investigated cases operated at φ < 0.40, the thermo-diffusive instabilities are able to almost double the laminar flame speed with reference to the unstretched one. However, under such conditions, it is also shown that the Karlovitz stretch factor (K), as computed by Bradley et al. [17,18] is higher than 0.1. Since K quantifies the relative impact of laminar (i.e. instabilities) and turbulent effects on wrinkling, high values of the parameter suggest that the flame speed enhancement can be effectively approximated as being entirely driven by turbulence. Therefore, for the operating conditions investigated in Ref. [35] and in the present paper, the impact of the thermo-diffusive instabilities on the capabilities of the framework to correctly predict engine performance can be considered of secondary importance. This is not in contrast with the existing literature. Although recent fundamental works [12,14] highlight the influence of the TD instabilities at engine-like conditions, many applicative works [20,23,24,26,71–74] carried out in the past obtain reasonable results neglecting them. This suggests that the actual influence of the instabilities on engine performance can vary from case to case. It is also important to point out that, in these considerations, only the impact of the TD instabilities on engine performance is considered. Other effects such as on NO_x emissions are neglected at this stage.

Before moving to the next section, it is useful to highlight that the only calibration parameters used in the simulations are the r_k threshold value for the ignition model and the constant A for the combustion one. The values used in the present work are the same throughout the

Table 2
Pressure, temperature and equivalence ratio found at the spark time for each case. The values are average quantities over a gas volume at the spark-plug. The laminar flame thickness calculated from the 1D computations, and the resulting kernel radius are reported as well.

Case number	p [bar]	T [K]	φ [−]	δ_l [mm]	$r_{k,init}$ [mm]
1	11.4	732	0.30	0.168	0.220
2	11.4	732	0.35	0.096	0.151
3	11.4	732	0.40	0.068	0.120
4	11.4	732	0.45	0.056	0.106
5	11.4	732	0.50	0.05	0.098
6	11.4	732	0.55	0.049	0.097
7	14.4	722	0.30	0.191	0.240
8	14.4	722	0.35	0.098	0.153
9	14.4	722	0.40	0.066	0.118
10	14.4	722	0.45	0.05	0.098
11	10.8	681	0.35	0.127	0.182
12	11.6	711	0.40	0.072	0.125
13	11.9	731	0.45	0.054	0.103
14	12.8	743	0.50	0.045	0.091
15	12.8	752	0.55	0.043	0.089

operating points and, interestingly, they are very close to the ones adopted in a previous work carried out with the same framework but on a completely different engine [34,35]. However, despite the robustness of the framework (as it will be pointed out in the result section), the values of the calibration parameters are expected to be valid as long as the proposed framework is not modified. For example, changing the laminar flame speed correlation may drive a (minimal) re-calibration of the parameters.

Another aspect to point out is that, although only two close revving speeds are analysed, the equivalence ratio range of the operating points is quite wide, leading to laminar flame speed values spanning three orders of magnitude. Therefore, even if a narrow range of turbulence levels is investigated, actually very different values of the ratio between turbulence and chemistry scales are explored. This means that the Damköhler-like correlation is validated against a wide distribution of points in the Borghi-Peters diagram. This aspect will be better detailed and discussed in the results section.

Finally, an overview on the computational mesh is given (see Fig. 4). It is composed by nearly 600 k cells at the bottom dead centre (BDC), with a minimum size of 0.6 mm and a maximum of 1.2 mm. A refinement around the spark plug is present, with halved cell size. A prismatic layer of 0.3 mm thickness is present on all the solid surfaces. This mesh is created based on the authors' experience on in-cylinder simulations and then verified by a sensitivity reported in Ref. [35].

4. Results

As previously anticipated, H_2 is port injected far from the intake valves to obtain a homogeneous mixture inside the cylinder. Accordingly, the mixture at the intake boundary of the domain is assumed to be perfectly premixed. In terms of modelling, the experimental injection strategy allows the focus to be placed on combustion rather than on injection and mixing processes. Therefore, cold flow results are not presented in the following and the discussion is entirely focused on the combustion outcomes. In the first paragraph, numerical pressure traces are compared to the experimental counterparts for each of the investigated cases. Comparisons in terms of combustion indicators and flame imaging are also proposed.

In the second paragraph, the combustion regimes characterising the investigated cases are analysed.

4.1. Numerical-experimental comparison

In the present section, the predictive capabilities of the proposed approach are proven. At first, a numerical-experimental comparison in terms of pressure traces is proposed. The comparison starts with the φ sweep at 0.7 bar of intake pressure, which is reported in Fig. 5a). Then Fig. 5c) and e) show the φ sweeps at 0.9 bar and constant IMEP. Overall, a strong agreement between CFD and experimental outcomes is found. The main discrepancies deal with the pressure peak for some cases. In particular, major underpredictions (but always lower than 1.3 bar) are noticed in the $\varphi = 0.45$ case of the 0.7 bar sweep, in the $\varphi = 0.40$ case of the 0.9 bar sweep and in the $\varphi = 0.35$ case of the constant IMEP sweep. A more detailed comparison between CFD and experiments is obtained by the apparent heat release rate (AHRR) traces reported in Fig. 5b), d) and 5f). An overall agreement is confirmed, even if discrepancies are identified also for this quantity. In particular, the main differences between numerical and experimental values are observed in correspondence of the AHRR peaks and towards the combustion completion, where the numerical traces are, for most cases, too inflated with respect to the experimental ones. The reason for this overestimation is multiple. Firstly, flame quenching at the walls is not modelled at this stage of numerical framework development. The effect can be non-negligible during the combustion completion, when the flame is close to the chamber walls. Secondly, the blow-by is not considered in the simulations even if slightly present in the experiments. Thirdly, although the boundary conditions derive from the experimental measurements, minimal errors in the numerical trapped mass of the different cases are present. Fourthly, the adopted heat transfer model is widely tested on gasoline and Diesel engines but no validation is available for H_2 ICEs. Although it should be able to account for the mixture properties (thanks to variable Prandtl number inside the thermal wall function), the low quenching distance characterising H_2 combustion may require ad hoc modification of the model. Anyway, despite the overestimations in terms of total heat release in some operating conditions, the overall agreement between simulations and experiments is not remarkably affected.

For a more quantitative comparison between CFD and experiments, combustion indicators (MFB, mass of fuel burnt) are reported in Fig. 6, where MFB 0–10, MFB 50 (combustion timing) and MFB 10–90 (combustion duration) are proposed. They are CA intervals between spark-time and 10 % of MFB, between spark-time and 50 % of MFB and between 10 % and 90 % of MFB, respectively. Combustion timing is properly captured, as demonstrated by the MFB 50 plots. The error between numerical and experimental values is reported and is shown to be minimal. Greater gaps can be noticed for MFB 0–10 and MFB 10–90. As for the latter, the overall tendency throughout the sweeps is to underestimate the combustion duration for the lower equivalence ratios, because of inaccuracies in the combustion completion prediction. This is mainly related to the flame-wall interaction, which is not modelled here. In fact, very lean mixtures are more sensitive to flame quenching at the end of the combustion while approaching the walls. Conversely, by increasing the equivalence ratio, the sensitivity is lower and the CFD outcomes are more accurate compared to the experimental counterparts.

As a further validation, a comparison in terms of imaging is also proposed. In Fig. 7, the experimental flame images are compared with

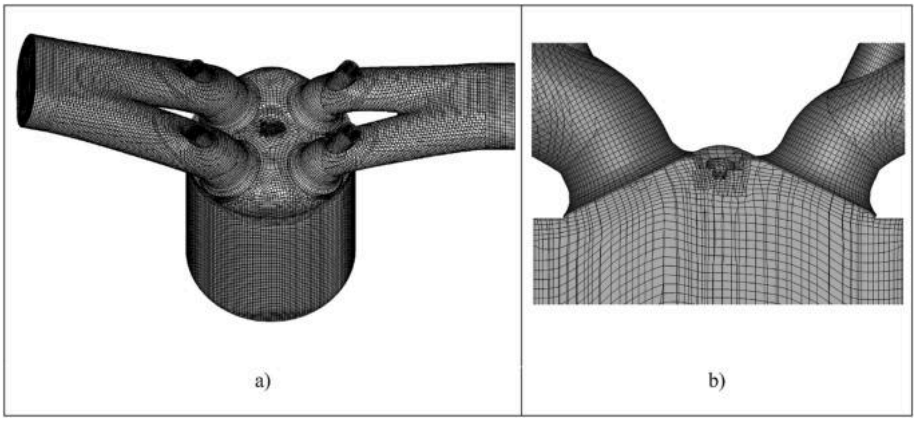

Fig. 4. Computational grid a) with a detail of the spark refinement b).

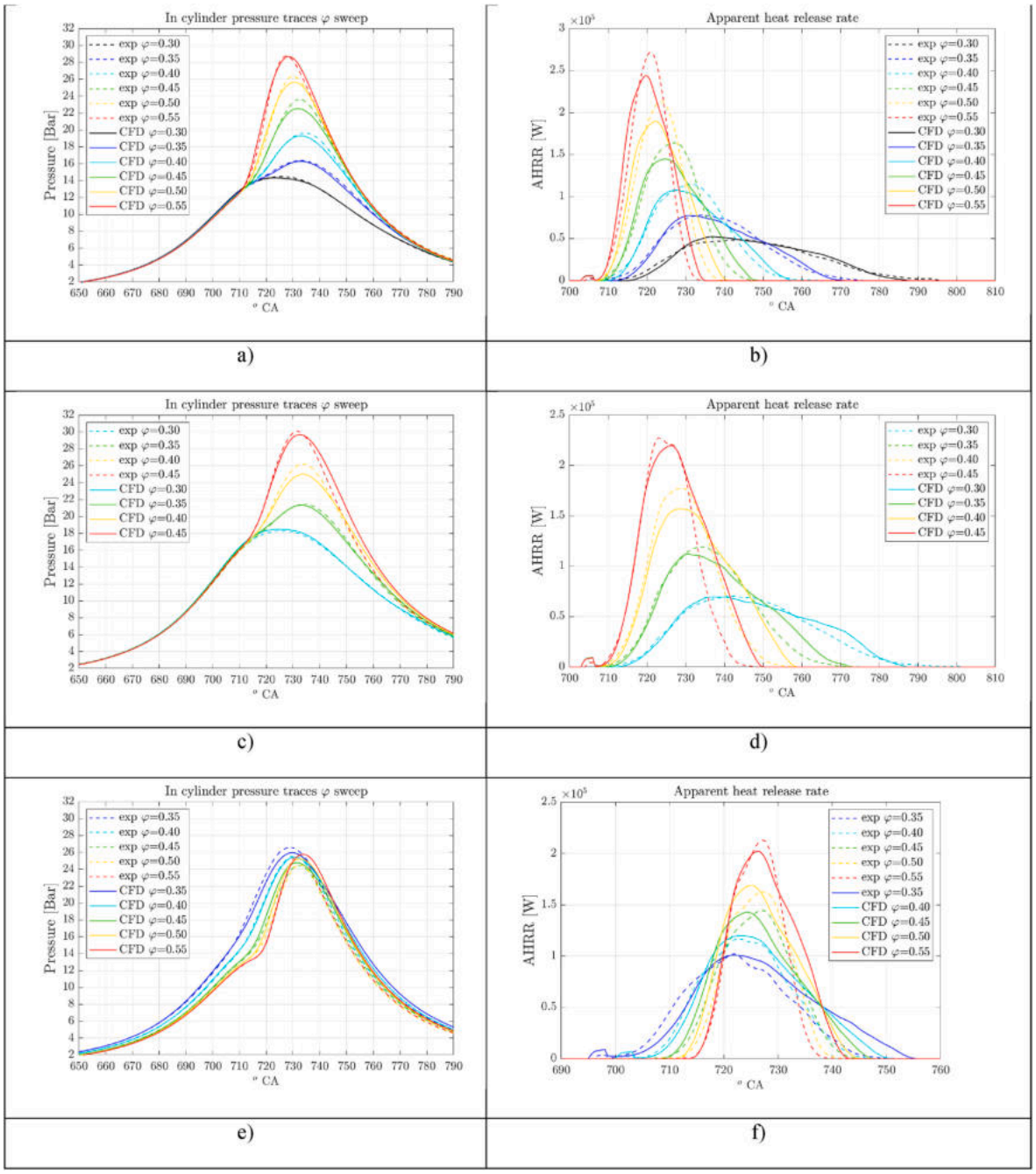

Fig. 5. Numerical-experimental comparison in terms of pressure traces and AHRR at intake pressure of 0.7 bar (a and b), intake pressure of 0.9 bar (c and d) and constant IMEP (e and f).

the calculated G = 0 isosurface, for the φ sweep at intake pressure of 0.7 bar. Only this sweep is considered for the comparison, as experimental images are not available for the other operating conditions. In each row, three different CAs are compared: 709°, 715° and 721°. 709° is the minimum CA at which the flame kernel is visible in the φ = 0.30 case, while 721°CA is the maximum one before the flame expands beyond the optical window in the φ = 0.55 case. 715° CA is purposely chosen as in the middle of the previously considered values. Overall, the numerical representations closely resemble the experimental images. A more detailed discussion of the imaging is proposed in the following.

Considering the combustion indicators presented in Fig. 6, the MFB 0–10 is roughly 16° CA for the φ = 0.40 case and 10° CA for the φ = 0.55 one. Therefore, the 10 % of MFB occurs at about 721°CA and 715°CA, respectively. Not by chance, observing the images of Fig. 7, φ = 0.40 case at 721° CA and φ = 0.55 one at 715° CA show a similar flame position. In addition, the previously discussed increasing overestimation of the MFB 0–10 obtained by lowering the equivalence ratio is confirmed by the images, that show a predicted flame radius smaller than the experimental counterpart at φ = 0.30 and φ = 0.35.

In order to perform a quantitative comparison, Fig. 8a) reports a plot of the flame radius as a function of the CA, while Fig. 8b) its time derivative. The radius is computed as the one of the circle characterised by the same perimeter of the flame contour. The equivalent radius is calculated using the same method for both numerical and experimental images. The solid lines are the ensemble average experimental data, with the semi-transparent area representing a ±2σ deviation. The computed data are reported with dotted lines. The lines interrupt roughly in correspondence of the 5 % of burnt mass. As the flame radius

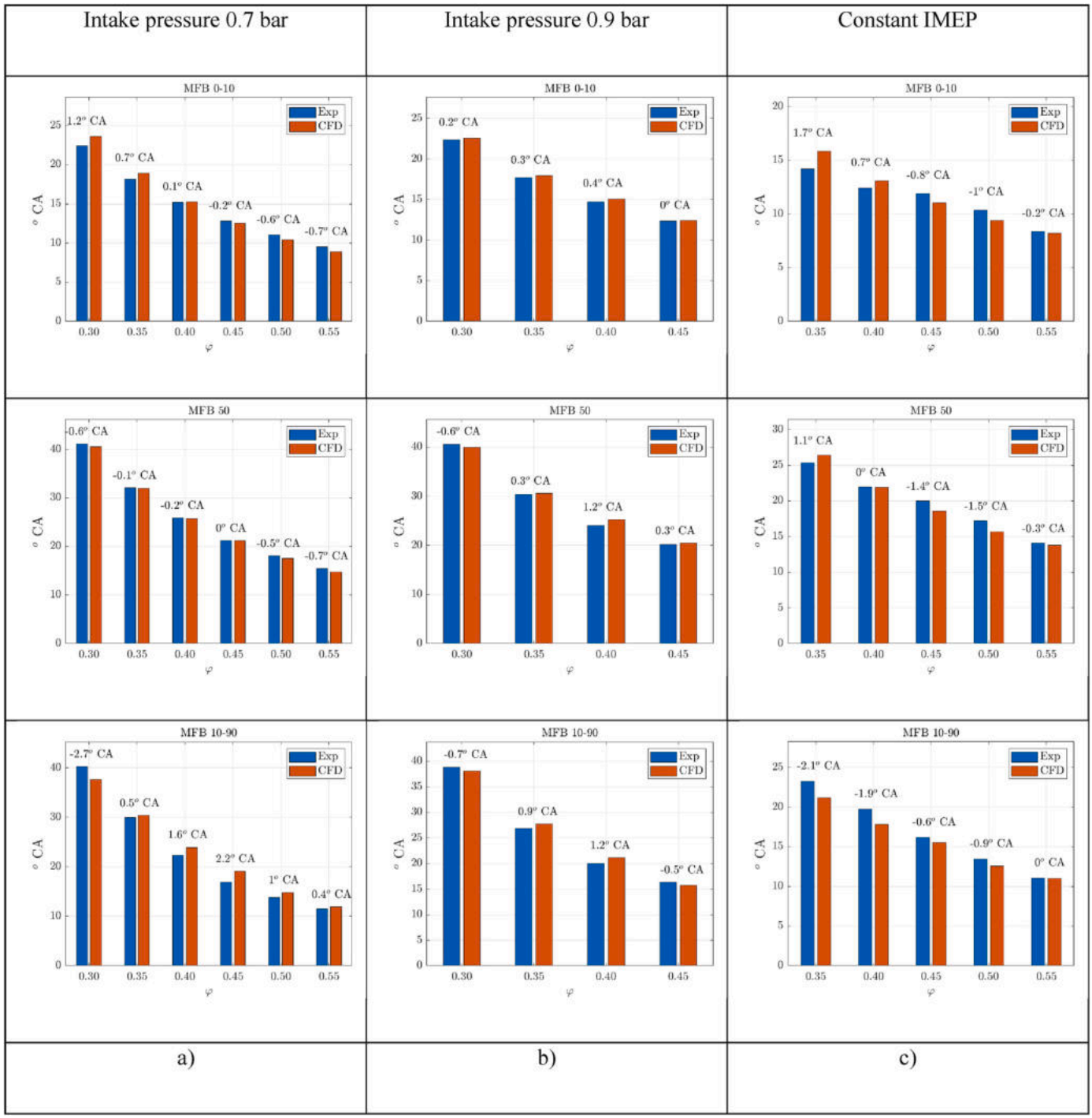

Fig. 6. Comparison of combustion indicators (MFB 0–10, MFB 50 and MFB 10–90) for a) the φ sweep at intake pressure of 0.7 bar, b) the φ sweep at intake pressure of 0.9 bar and c) the φ sweep at constant IMEP.

evolution is almost linear in all the cases, two important factors should be considered: the slope of the lines and their shift. Before analysing such factors, it should be pointed out that, in the CFD framework, the ignition model switches off soon in the combustion process, i.e. at ~707°CA for the φ = 0.55 case and ~712°CA for the φ = 0.30. This means that the ignition model is mainly responsible for the shift, while the slope (i.e. combustion rate) is primarily related to the combustion model (intended as a combination of model itself and correlations of laminar and turbulent flame speeds). As visible in Fig. 8a) and confirmed by the derivative reported in Fig. 8b), the slope is reasonably captured, as proof of the reliability of the combustion model. All the numerical curves fall in the respective bands representing 95 % of the experimental traces. The main issues deal with the shifts of the traces, which are primarily accumulated during the ignition model activity periods. However, errors can be considered acceptable, even if there is room for improvement in the ignition modelling.

4.2. *Combustion regime*

The second section of the results is dedicated to a deepening of the combustion regimes characterising the investigated cases. Internal combustion engines often exhibit “flamelet” combustion, for which the

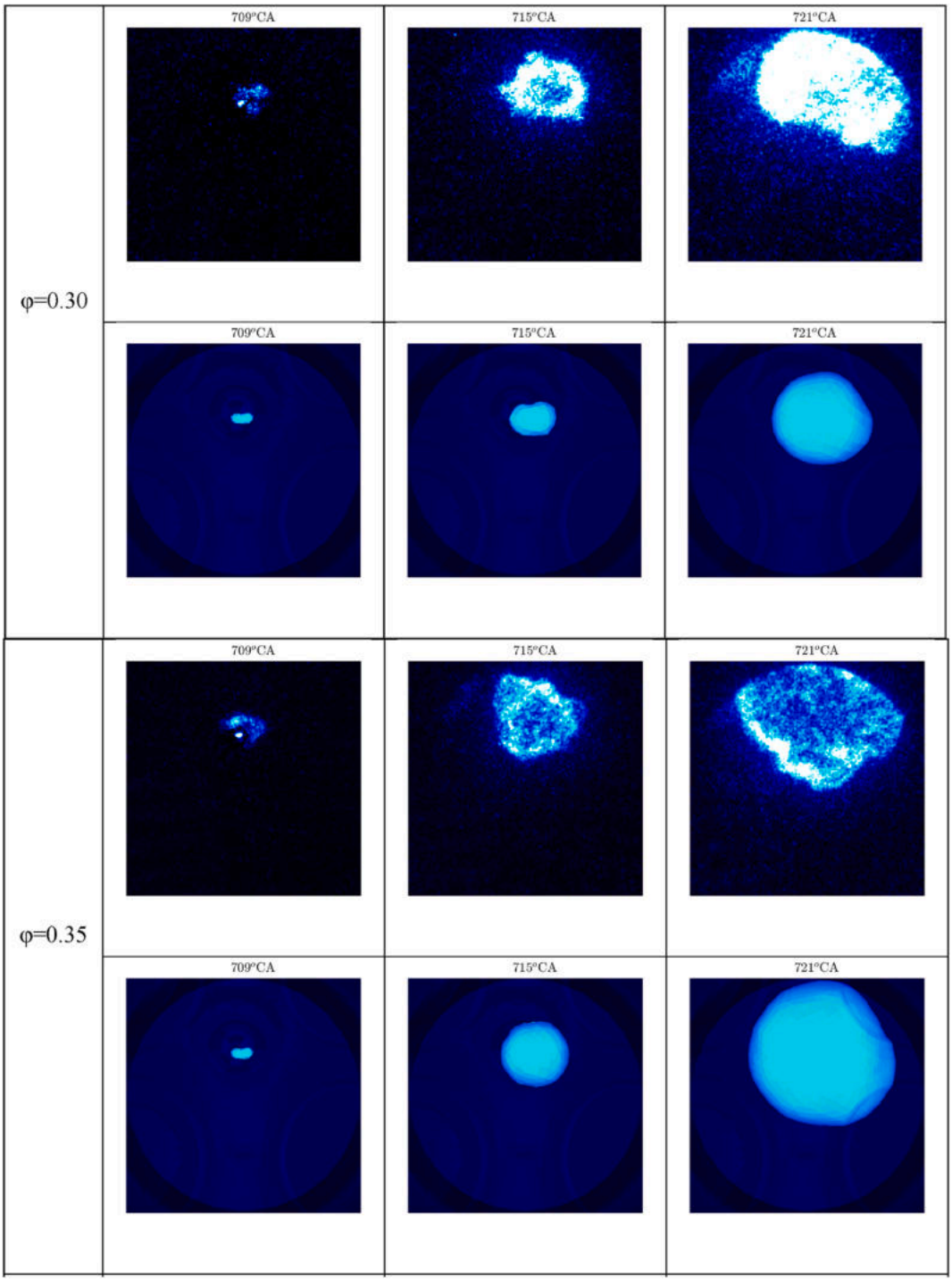

Fig. 7. Numerical-experimental comparison in terms of flame imaging at 709°CA, 715°CA, and 721°CA for each case of the φ sweep at intake pressure of 0.7 bar.

G-equation model (as implemented in the adopted software) is developed and widely adopted [69]. The goal of this section is, on the one hand, to confirm the presence of "flamelet" combustion in the investigated cases. On the other hand, it is necessary to examine the applicability of the consolidated combustion regime classification methods and to verify potential modifications proposed in the literature that can enhance their accuracy. The analysis is carried out by means of the Borghi-Peters diagram as presented in Ref. [69], since it is a well-consolidated tool to classify the combustion regimes of hydrocarbon fuels.

Before the results, it is important to emphasize that criteria commonly adopted with hydrocarbon fuels for classifying combustion regimes (also used in the Borghi-Peters diagram [69]) may be inadequate for hydrogen. For instance, one of the criteria is that the combustion regime moves from "flamelet" to "thin reaction zones" for Karlovitz number (Ka) greater than 1, i.e. above the so-called Klimov-Williams limit defined by the condition Ka = 1. This criterion is obtained through a series of assumptions [75,76], among which Lewis number equal to 1, which is not the case of lean H_2/air mixtures. If the hypotheses are not respected, the combustion classification can be

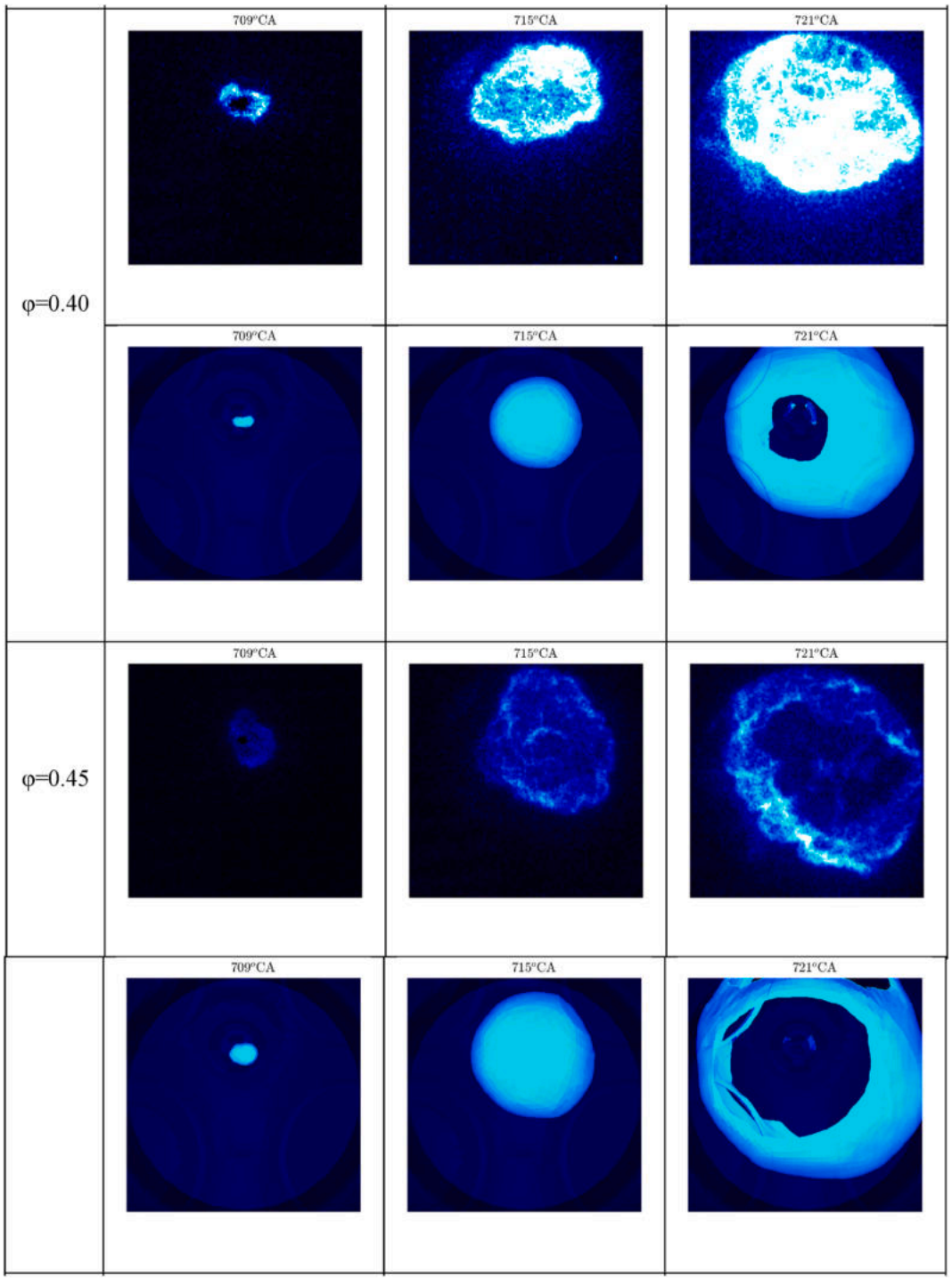

Fig. 7. (*continued*).

misleading. This is confirmed by Aspden et al. in Ref. [77], who vary the equivalence ratio of a lean hydrogen-air mixture (and, so, the Lewis number) and, although the Damköhler (Da) and Karlovitz numbers are kept constant, the combustion regime shifts from "thin reaction zone" to "broken reaction zones". The findings proposed by Aspden et al. point out the limitations of the combustion regime classification proper of hydrocarbon fuels when applied to lean hydrogen combustion. In response, the same authors propose a modification to the classical definitions of Da and Ka, by computing these numbers via freely propagating flame properties instead of laminar ones. This approach allows them to obtain coherent results, i.e. when varying the Lewis number while keeping Ka and Da constant, the DNS simulations consistently exhibit the same combustion regime across the different conditions. This means that, by adopting ad-hoc definitions of Da and Ka, the Borghi-Peters diagram could be still adopted for classification of combustion regimes.

In the light of the discussion above, in the present paper the Borghi-Peters diagram is presented both in its original form and in the modified version based on the approach proposed by Aspden [77]. The comparison between original and modified diagrams is shown in Fig. 9. The modified ones feature different axis names, where the additional subscript 'F' indicates the freely propagating flame properties. Such

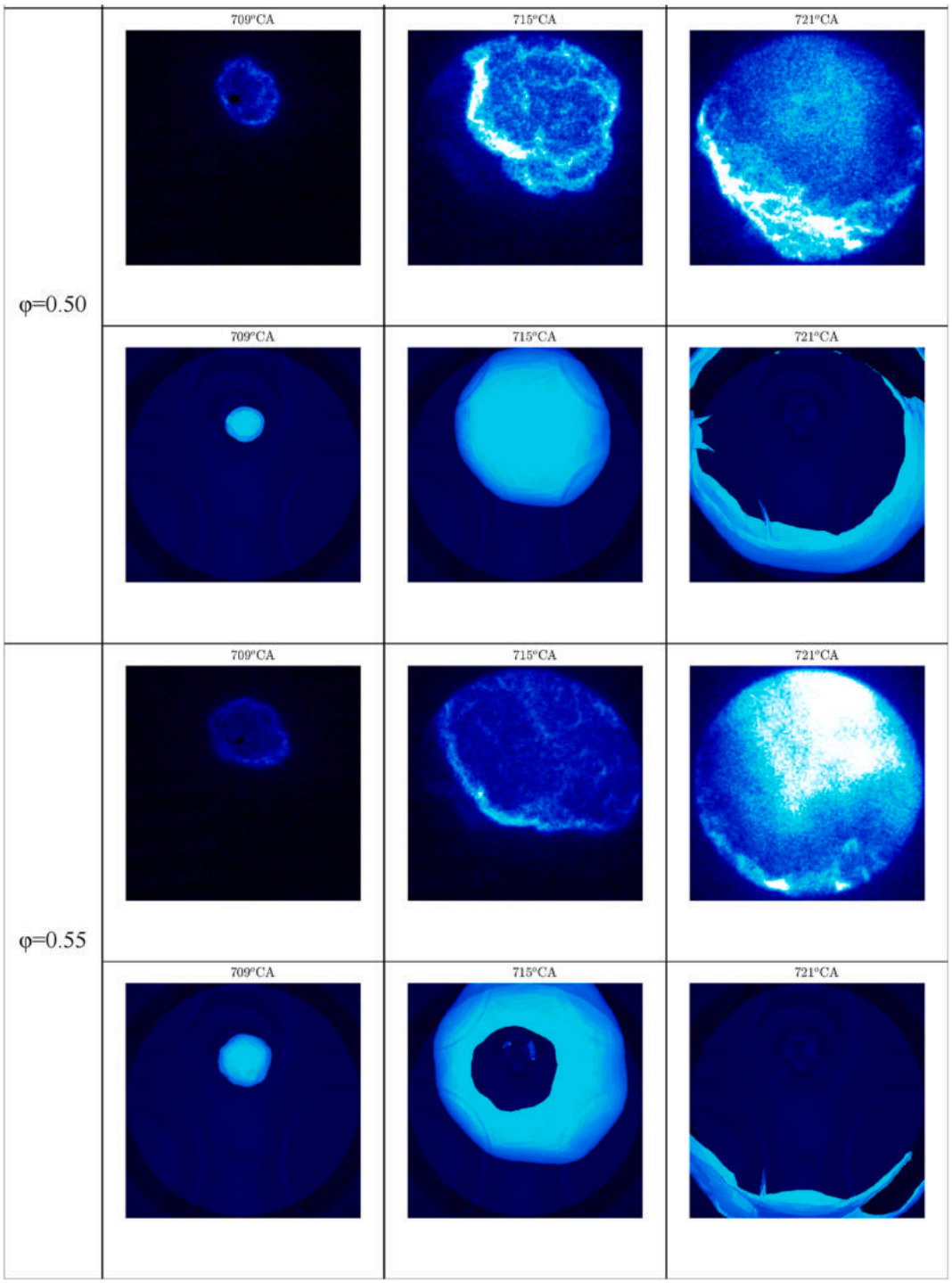

Fig. 7. (*continued*).

properties, namely laminar flame speed and thickness, are computed through the correlations proposed by Howarth [16]. For completeness, in each operating condition, the initial marked point represents the combustion start and the line is the evolution of the regime during the combustion process. Each point of the line represents a different CA and it is obtained by calculating the average combustion regime on the reaction zone. It can be observed that both versions of the diagram cover a wide range of conditions, although the spread is narrower in the corrected version. In both the diagrams, the combustion traces extend beyond the formal applicability limits of G-equation. However, the corrected version exhibits an overall shift of the traces toward the "flamelet" combustion regime. For instance, the two cases at $\varphi = 0.35$ move from being entirely within the thin reaction zones to partially entering the "flamelet" regime.

Although the use of the adopted combustion model is not strictly valid given the results proposed in Fig. 9, G-equation combined to a Damköhler-like correlation is able to reliably predict the combustion evolution for all the investigated cases, as demonstrated in the previous paragraph. This capability is confirmed by experimental observations of the authors of the present paper on the same engine. In the experiments proposed in Ref. [9] and carried out at 1200 rpm, with φ values from 0.25 to 0.55, a wide range of conditions is covered. As a consequence,

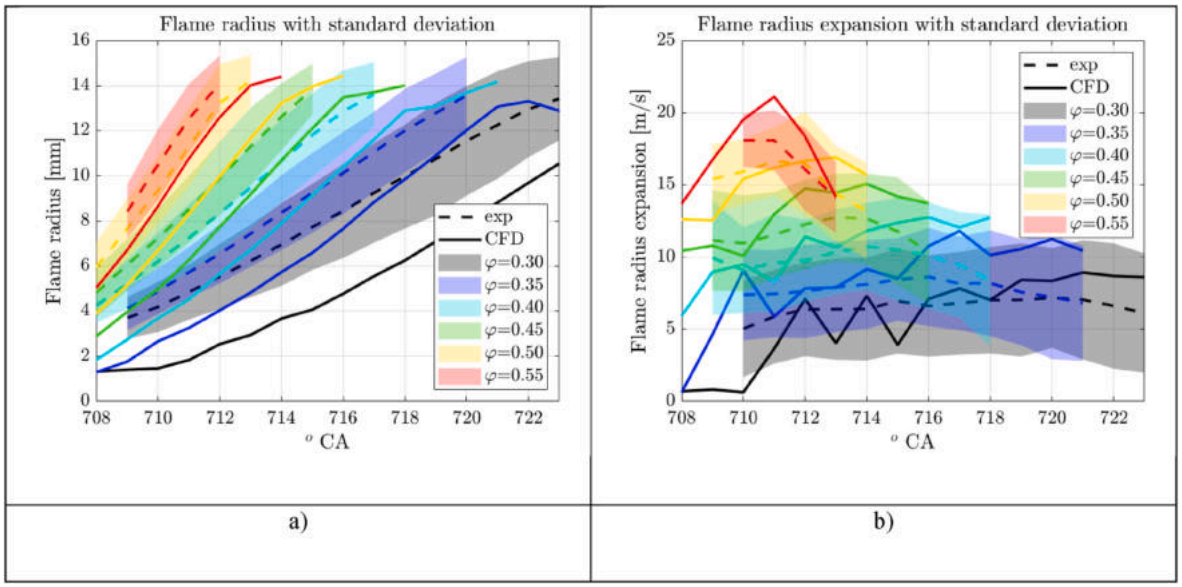

Fig. 8. a) flame radius and b) flame radius time derivative, both as a function of crank angle, for each case of the φ sweep at intake pressure of 0.7 bar. Numerical data (solid lines) are compared with experimental ones (dotted lines), with the latter including a ±2σ band.

although the corrections move all the operating points outside the "broken reaction zones" regime, the flame occupies different regions of both the original and modified Borghi-Peters diagrams. As for the Karlovitz number, the original and modified formulations span four and three orders of magnitude (from 0.025 to 178 and from 0.034 to 70), respectively. Despite the very different conditions, the authors show that the behaviour of the flame can be represented by a single Damköhler--like correlation, similarly to the numerical simulations. More in detail, Fig. 10a) and 10b) show the original and modified Borghi-Peters diagrams with the experimentally investigated conditions. Each point represents an operating condition, and it is calculated when the flame front has an equivalent radius of 8 mm. For the calculation of the points (i.e. the positioning inside the diagram), the flame speed and thickness are computed trough a kinetic solver, using the Burke mechanism. The turbulence intensity u' is estimated using the Heywood method [78], that provides values well aligned with the ones obtained by 3D-CFD simulations. The Heywood method is based on a correlation between mean piston velocity and turbulence intensity measured experimentally via laser Doppler anemometry. The integral length scale L_t is computed by particle image velocimetry (PIV) measurements across different CA and on different planes, and it coincides with the integral of the autocorrelation of the velocity field between zero and the first zero-crossing, as suggested by Pope [79]. A more detailed description of the experimental aspects can be found in Ref. [80].

For each of the points of Fig. 10, it is possible to correlate the ratio between turbulent flame speed directly measured through the optical window and laminar flame speed S_l with the quantity u'/S_l, by adopting the Damköhler-like correlation presented in Fig. 11a), where the constants A and n are shown as well. The turbulent flame speed is estimated as $\frac{\rho_b}{\rho_u}\cdot\overline{v_t}$, where the fraction is the ratio of the burnt density to the unburnt one and $\overline{v_t}$ is the measured flame expansion velocity computed by the flame images. In Fig. 11a), it is evident that a single correlation is able to properly fit all the experimentally-derived values and this is true considering also the modified quantities, as visible in Fig. 11b). Moreover, apart from the coefficients, the correlation is de facto coincident with the one adopted on the CFD side. In this regard, by comparing the experimentally-derived coefficients to those used in the numerical simulations, the exponent n values are similar. Conversely, A coefficient non-negligibly differs. The reasons for the discrepancy are multiple. For instance, laminar flame speed computation methods differ between experimental activity and 3D-CFD simulation. The former relies on the Burke mechanism, while the latter exploits the Konnov one. Anyway, regardless of the differences in the coefficients, the most important aspect is that both CFD and experiments agree on the fact that a single correlation to be formally adopted for "flamelet" combustion can be proficiently adopted at different regimes. This apparent contradiction can be explained in two different ways. Firstly, it is possible that the modifications proposed by Aspden are still not sufficient to obtain a proper classification of the combustion regime. Therefore, all the investigated conditions may actually fall in the "flamelet" regime. A second explanation can be due to the fact that, since the adopted Damköhler-like correlation is able to match the flame speeds in both "flamelet" and "thin reaction zones" regimes, the use of that expression within G-equation leads to proper predictions in both areas of the Borghi-Peters diagram. In other words, it is the capability (thanks to shape and/or tuning) of the turbulent flame speed correlation that compensates the deficiency of G-equation in the "thin reaction zones" regime. This clarification will be addressed in a future work.

Before presenting the conclusions, it is worth noting that the experimental fitting shown in Fig. 11 (whose validity may be reasonably extended at ultra-lean conditions, i.e. out of the "flamelet" regime, as discussed above) does not account for TD instabilities. Therefore, the proposed experiments seem to support the numerical evidence that, at the investigated conditions, combustion indicators can be accurately matched without considering TD instabilities. As anticipated in the numerical setup section, the main reason is related to the turbulence impact on the flame which overcomes the TD instability one.

5. Conclusions

In the last years, the interest in hydrogen as a green fuel for internal combustion engines has revamped. In fact, it represents a potential solution to achieve carbon neutrality while keeping a well-established technology. In this context, numerical simulations represent a powerful tool to support manufacturers in the design of efficient low-NO_x-emission engines. However, effective (i.e. predictive) simulation tools are needed for the scope. This is the reason why, in the present paper, a 3D-CFD approach including detailed modelling of ignition and combustion for the simulation of H_2 ICEs is proposed. An extensive validation on 15 operating points covering a wide spectrum of combustion regimes is carried out. The framework predictivity is assessed against experimental data and discussed, highlighting capabilities as well as

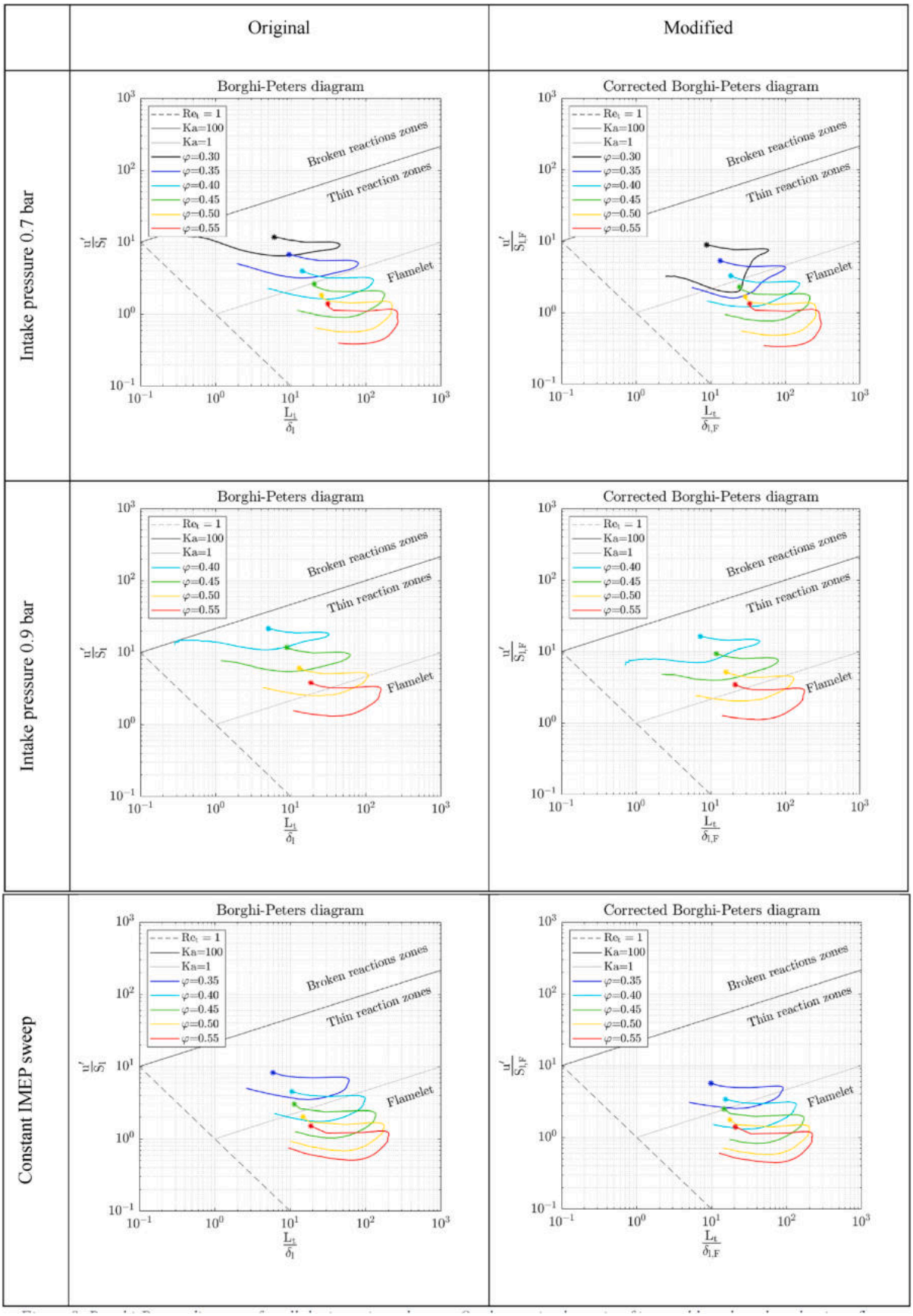

Fig. 9. Borghi-Peters diagrams for all the investigated cases. On the x-axis, the ratio of integral length scale to laminar flame thickness L_t/δ_l is reported, while the ratio between turbulent velocity fluctuations and laminar flame speed u'/S_l is reported on the y-axis.

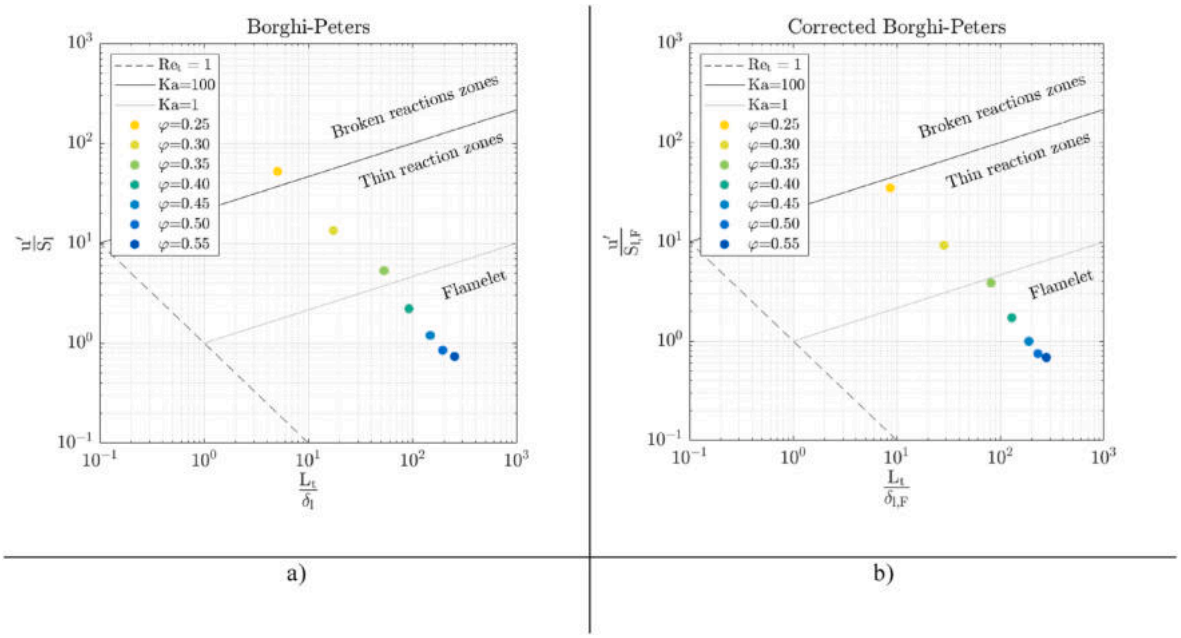

Fig. 10. Original a) and modified b) Borghi-Peters diagrams for the experimentally tested conditions.

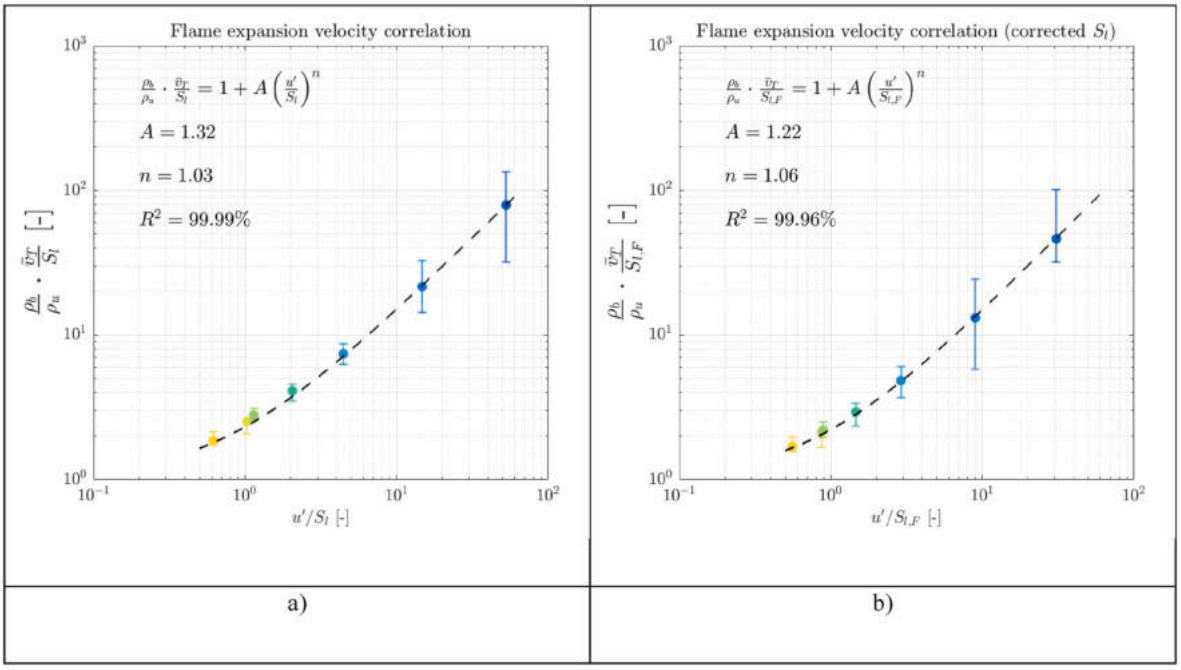

Fig. 11. Damköhler-like fitting for the experimentally-measured flame expansion speed values. Different colours are related to different equivalence ratios, as described in the legend of Fig. 10. The fitting is proposed for both original a) and modified b) quantities. (For interpretation of the references to colour in this figure legend, the reader is referred to the Web version of this article.)

limitations. On the one hand, the potential of the combustion model is proven as it is able to accurately capture both combustion phasing and duration (namely MFB 50 and MFB 10–90). On the other hand, even though the disagreement between CFD and experiments is minimal, it is shown that there is room for improvement in the flame kernel evolution representation. In other words, the ignition model can be further refined.

Overall, the results show a satisfying agreement between numerical outcomes and experimental counterparts. Therefore, the present activity demonstrates that a relatively simple framework can be proficiently employed for the prediction of H_2 ICE performance even at ultra-lean conditions, where aspects such as thermo-diffusive instabilities and combustion regimes can be critical. In fact, at the investigated ultra-lean mixtures, the thermo-diffusive instabilities have an influence so strong that the laminar flame speed can achieve values even twice the unstretched one [35]. Moreover, at very low φ, the conditions are such that, considering the Borghi-Peters diagram, the combustion does not pertain to the "flamelet" regime. Nonetheless, the 3D-CFD framework based on G-equation (i.e. a "flamelet" model) and correlations for laminar and turbulent flame speeds that do not account for TD instability effects is able to provide results in agreement with the experiments.

As a final remark, it should be noted that these conclusions are valid as long as the conditions are similar to those investigated in the present analysis. On the one hand, the tested points cover a wide range of conditions that can be present in ICEs. On the other hand, the authors do not rule out the possibility of encountering operating conditions in which, for instance, instabilities become predominant and require adequate modelling.

In conclusion, the proposed framework is proven to be effective, so it can be proficiently adopted to support the work by the designers to develop new generation H_2-ICEs.

CRediT authorship contribution statement

Stefano Sfriso: Writing – original draft, Investigation, Formal analysis. **Fabio Berni:** Writing – review & editing, Validation, Supervision. **Caio Ramalho Leite:** Investigation, Formal analysis, Data curation. **Sebastiano Breda:** Writing – review & editing, Validation. **Fabriche Foucher:** Investigation, Data curation, Conceptualization. **Pierre Brequigny:** Investigation, Formal analysis, Data curation. **Jacques Borée:** Investigation, Data curation, Conceptualization. **Stefano Fontanesi:** Writing – review & editing, Supervision, Software.

Declaration of competing interest

The authors declare that they have no known competing financial interests or personal relationships that could have appeared to influence the work reported in this paper.

Acknowledgments

The experimental work described in this paper has been conducted by Caio Ramalho Leite, Pierre Brequigny, and Fabrice Foucher from the University of Orléans.

The authors gratefully acknowledge the University of Modena and Reggio Emilia for supporting the activity by the "Fondo di Ateneo per la Ricerca 2024 per il finanziamento di piani di sviluppo dipartimentale nell'ambito della ricerca" (FAR 2024), the Agence Nationale de Recherche for the grant number 20-CE05-0007 (ALEKCIA ANR project) and the "PIANO NAZIONALE DI RIPRESA E RESILIENZA (PNRR) – MISSIONE 4 COMPONENTE 2, "Dalla ricerca all'impresa" INVESTIMENTO 1.4, Potenziamento strutture di ricerca e creazione di "campioni nazionali di R&S" su alcune Key Enabling Technologies, finanziato dall'Unione europea – NextGenerationEU - Progetto identificato con codice CN00000023. Titolo "Sustainable Mobility Center (Centro Nazionale per la Mobilità Sostenibile – CNMS)" - Spoke 12 - Avviso MUR 3138/2021 modificato con DD 3175/2021".

References

[1] Das L. Exhaust emission characterisation of hydrogen-operated engine system: nature of pollutants and their control techniques. Int J Hydrogen Energy 1991;16 (11):765–75. https://doi.org/10.1016/0360-3199(91)90075-T.
[2] Regulation (EU) 2023/851 OF the EUROPEAN parliament and OF the COUNCIL," Official Journal of the European Union, OJ L 110.
[3] Larson ED. A review of life-cycle analysis studies on liquid biofuel systems for the transport sector. Energy Sustain Dev Jun. 2006;10(2):109–26. https://doi.org/10.1016/S0973-0826(08)60536-0.
[4] Luo Q, et al. Experimental investigation of combustion characteristics and NOx emission of a turbocharged hydrogen internal combustion engine. Int J Hydrogen Energy Feb. 2019;44(11):5573–84. https://doi.org/10.1016/j.ijhydene.2018.08.184.
[5] Marwaha A, Subramanian KA. Experimental investigations of effects of cycle time on NOx emission in a hydrogen fueled multi-cylinder automotive spark ignition engine. Sustain Energy Technol Assessments Aug. 2022;52:102203. https://doi.org/10.1016/j.seta.2022.102203.
[6] Luo Q, Sun B. Experiments on the effect of engine speed, load, equivalence ratio, spark timing and coolant temperature on the energy balance of a turbocharged hydrogen engine. Energy Convers Manag Apr. 2018;162:1–12. https://doi.org/10.1016/j.enconman.2017.12.051.
[7] Tsujimura T, Suzuki Y. Development of a large-sized direct injection hydrogen engine for a stationary power generator. Int J Hydrogen Energy Apr. 2019;44(22): 11355–69. https://doi.org/10.1016/j.ijhydene.2018.09.178.
[8] Ramalho Leite C, Laignel M, Brequigny P, Borée J, Foucher F. Experimental combustion analysis in a gasoline baseline hydrogen-fueled internal combustion engine at ultra-lean conditions. In: SAE technical papers. SAE International; Aug. 2023. https://doi.org/10.4271/2023-24-0073.
[9] Ramalho Leite C, Brequigny P, Borée J, Foucher F. Early flame development characterisation of ultra-lean hydrogen–air flames in an optical spark-ignition engine. Proc Combust Inst 2024;40(1–4):105260. https://doi.org/10.1016/j.proci.2024.105260.
[10] Fontanesi S, Postrioti L, Magnani M, Martino M, Brizi G, Cicalese G. Preliminary assessment of hydrogen direct injection potentials and challenges through a joint experimental and numerical characterisation of high-pressure gas jets. In: SAE technical papers. SAE International; Sep. 2022. https://doi.org/10.4271/2022-24-0014.
[11] Postrioti L, Martino M, Fontanesi S, Breda S, Magnani M. Experimental and numerical momentum flux analysis of jets from a hydrogen injector. In: SAE technical papers. SAE International; Apr. 2024. https://doi.org/10.4271/2024-01-2616.
[12] Berger L, Attili A, Pitsch H. Intrinsic instabilities in premixed hydrogen flames: parametric variation of pressure, equivalence ratio, and temperature. Part 2 – non-linear regime and flame speed enhancement. Combust Flame Jun. 2022;240: 111936. https://doi.org/10.1016/j.combustflame.2021.111936.
[13] Berger L, Attili A, Gauding M, Pitsch H. Effects of Karlovitz number variations on thermodiffusive instabilities in lean turbulent hydrogen jet flames, vol. 40. Proceedings of the Combustion Institute; 2024, 105219. https://doi.org/10.1016/j.proci.2024.105219. 1–4.
[14] Berger L, Attili A, Pitsch H. Synergistic interactions of thermodiffusive instabilities and turbulence in lean hydrogen flames. Combust Flame Oct. 2022;244:112254. https://doi.org/10.1016/j.combustflame.2022.112254.
[15] Howarth TL, Aspden AJ. An empirical characteristic scaling model for freely-propagating lean premixed hydrogen flames. Combust Flame Mar. 2022;237: 111805. https://doi.org/10.1016/j.combustflame.2021.111805.
[16] Howarth TL, Hunt EF, Aspden AJ. Thermodiffusively-unstable lean premixed hydrogen flames: phenomenology, empirical modelling, and thermal leading points. Combust Flame Jul. 2023;253:112811. https://doi.org/10.1016/j.combustflame.2023.112811.
[17] Bradley D, Gaskell PH, Gu XJ, Sedaghat A. Premixed flamelet modelling: factors influencing the turbulent heat release rate source term and the turbulent burning velocity. Combust Flame Nov. 2005;143(3):227–45. https://doi.org/10.1016/j.combustflame.2005.05.014.
[18] Bradley D, Lawes M, Liu K, Mansour MS. Measurements and correlations of turbulent burning velocities over wide ranges of fuels and elevated pressures. Proc Combust Inst 2013;34(1):1519–26. https://doi.org/10.1016/j.proci.2012.06.060.
[19] Liu X, et al. Hydrogen pre-chamber combustion at lean-burn conditions on a heavy-duty diesel engine: a computational study. Fuel Mar. 2023;335:127042. https://doi.org/10.1016/j.fuel.2022.127042.
[20] Babayev R, Andersson A, Dalmau AS, Im HG, Johansson B. Computational characterisation of hydrogen direct injection and nonpremixed combustion in a compression-ignition engine. Int J Hydrogen Energy May 2021;46(35):18678–96. https://doi.org/10.1016/j.ijhydene.2021.02.223.
[21] Gerke U, Steurs K, Rebecchi P, Boulouchos K. Derivation of burning velocities of premixed hydrogen/air flames at engine-relevant conditions using a single-cylinder compression machine with optical access. Int J Hydrogen Energy Mar. 2010;35(6):2566–77. https://doi.org/10.1016/j.ijhydene.2009.12.064.
[22] Peters N. Laminar diffusion flamelet models in non-premixed turbulent combustion. Prog Energy Combust Sci Jan. 1984;10(3):319–39. https://doi.org/10.1016/0360-1285(84)90114-X.
[23] Pielecha I, Merkisz J, Urbański P, Gallas D, Andrych-Zalewska M. A numerical Study of the effect of hydrogen fuelled turbulent jet ignition engine. In: SAE technical papers. SAE International; Aug. 2022. https://doi.org/10.4271/2022-01-1007.
[24] Rouleau L, Duffour F, Walter B, Kumar R, Nowak L. Experimental and Numerical investigation on hydrogen internal combustion engine. In: SAE technical papers. SAE International; Sep. 2021. https://doi.org/10.4271/2021-24-0060.
[25] Maio G, et al. Experimental and numerical investigation of a direct injection spark ignition hydrogen engine for heavy-duty applications. Int J Hydrogen Energy Aug. 2022;47(67):29069–84. https://doi.org/10.1016/j.ijhydene.2022.06.184.
[26] Knop V, Benkenida A, Jay S, Colin O. Modelling of combustion and nitrogen oxide formation in hydrogen-fuelled internal combustion engines within a 3D CFD code. Int J Hydrogen Energy Oct. 2008;33(19):5083–97. https://doi.org/10.1016/j.ijhydene.2008.06.027.
[27] Hernandez I, Turquand D'Auzay C, Penning R, Shapiro E, Hughes J. Thermo-Diffusive flame speed adjustment and its application to hydrogen engines. In: SAE technical papers. SAE International; Apr. 2023. https://doi.org/10.4271/2023-01-0197.
[28] Sfriso S, et al. Combination of G-Equation and detailed Chemistry: an application to 3D-CFD hydrogen combustion simulations to predict NOx emissions in reciprocating internal combustion engines. Int J Hydrogen Energy Nov. 2024;89: 161–76. https://doi.org/10.1016/j.ijhydene.2024.09.252.
[29] Berni F, Pessina V, Teodosio L, d'Adamo A, Borghi M, Fontanesi S. An integrated 0D/1D/3D numerical framework to predict performance, emissions, knock and heat transfer in ICEs fueled with NH3–H2 mixtures: the conversion of a marine Diesel engine as case study. Int J Hydrogen Energy Oct. 2023. https://doi.org/10.1016/j.ijhydene.2023.09.158.

[30] Zimont VL. Gas premixed combustion at high turbulence. Turbulent flame closure combustion model. Exp Therm Fluid Sci Mar. 2000;21(1–3):179–86. https://doi.org/10.1016/S0894-1777(99)00069-2.
[31] Lipatnikov AN, Chomiak J. Turbulent flame speed and thickness: phenomenology, evaluation, and application in multi-dimensional simulations. Prog Energy Combust Sci Jan. 2002;28(1):1–74. https://doi.org/10.1016/S0360-1285(01)00007-7.
[32] Gülder ÖL. Turbulent premixed flame propagation models for different combustion regimes. Symposium (International) on Combustion Jan. 1991;23(1):743–50. https://doi.org/10.1016/S0082-0784(06)80325-5.
[33] Verhelst S, Tjoen C, Vancoillie J, Demuynck J. A correlation for the laminar burning velocity for use in hydrogen spark ignition engine simulation. Int J Hydrogen Energy Jan. 2011;36(1):957–74. https://doi.org/10.1016/j.ijhydene.2010.10.020.
[34] Sfriso S, Berni F, Fontanesi S, D'Adamo A, Antonelli M, Frigo S. A 3D-CFD numerical approach for combustion simulations of spark ignition engines fuelled with hydrogen: a preliminary analysis. In: SAE technical papers. SAE International; Apr. 2023. https://doi.org/10.4271/2023-01-0207.
[35] Sfriso S, et al. Proposal and validation of 3D-CFD framework for ultra-lean hydrogen combustion in ICEs. In: SAE technical papers. SAE International; Apr. 2024. https://doi.org/10.4271/2024-01-2685.
[36] Sfriso S, et al. Proposal and validation of a numerical framework for 3D-CFD in-cylinder simulations of hydrogen spark-ignition internal combustion engines. Int J Hydrogen Energy Jan. 2024;53:114–30. https://doi.org/10.1016/j.ijhydene.2023.12.027.
[37] Yakhot V, Orszag SA. Renormalization group analysis of turbulence. I. Basic theory. J Sci Comput 1986;1(1):3–51. https://doi.org/10.1007/BF01061452.
[38] STAR-CD methodology guide.
[39] Teodosio L, Berni F. Optimization via genetic algorithm of a variable-valve-actuation spark-ignition engine based on the integration between 1D/3D simulation codes and optimizer. Int J Engine Res 2022. https://doi.org/10.1177/14680874221099874.
[40] Berni F, et al. A zonal secondary break-up model for 3D-CFD simulations of GDI sprays. Fuel 2022;309(Feb). https://doi.org/10.1016/j.fuel.2021.122064.
[41] Iacovano C, Berni F, Barbato A, Fontanesi S. A preliminary 1D-3D analysis of the darmstadt research engine under motored condition. In: E3S web of conferences. EDP Sciences; Oct. 2020. https://doi.org/10.1051/e3sconf/202019706006.
[42] Sparacino S, Berni F, Riccardi M, Cavicchi A, Postrioti L. 3D-CFD simulation of a GDI injector under standard and flashing conditions. In: E3S web of conferences. EDP Sciences; Oct. 2020. https://doi.org/10.1051/e3sconf/202019706002.
[43] Sparacino S, Berni F, D'Adamo A, Krastev VK, Cavicchi A, Postrioti L. Impact of the primary break-up strategy on the morphology of GDI sprays in 3D-CFD simulations of multi-hole injectors. Energies Jul. 2019;12(15). https://doi.org/10.3390/en12152890.
[44] Berni F, et al. Modeling of gaseous emissions and soot in 3D-CFD in-cylinder simulations of spark-ignition engines: a methodology to correlate numerical results and experimental data. Int J Engine Res 2022. https://doi.org/10.1177/14680874221112564.
[45] Berni F, Cicalese G, Borghi M, Fontanesi S. Towards grid-independent 3D-CFD wall-function-based heat transfer models for complex industrial flows with focus on in-cylinder simulations. Appl Therm Eng May 2021;190. https://doi.org/10.1016/j.applthermaleng.2021.116838.
[46] Berni F, Fontanesi S. A 3D-CFD methodology to investigate boundary layers and assess the applicability of wall functions in actual industrial problems: a focus on in-cylinder simulations. Appl Therm Eng 2020;174(Jun). https://doi.org/10.1016/j.applthermaleng.2020.115320.
[47] Berni F, Cicalese G, Sparacino S, Cantore G. On the existence of universal wall functions in in-cylinder simulations using a low-Reynolds RANS turbulence model. In: AIP conference proceedings. American Institute of Physics Inc.; Dec. 2019. https://doi.org/10.1063/1.5138752.
[48] Cicalese G, Berni F, Fontanesi S. Integrated in-cylinder/CHT methodology for the simulation of the engine thermal field: an application to high performance turbocharged DISI engines. SAE Int J Engines Apr. 2016;9(1):601–17. https://doi.org/10.4271/2016-01-0578.
[49] Berni F, Cicalese G, Fontanesi S. A modified thermal wall function for the estimation of gas-to-wall heat fluxes in CFD in-cylinder simulations of high performance spark-ignition engines. Appl Therm Eng 2017;115:1045–62. https://doi.org/10.1016/j.applthermaleng.2017.01.055.
[50] Cicalese G, Berni F, Fontanesi S, D'Adamo A, Andreoli E. A comprehensive CFD-CHT methodology for the characterisation of a diesel engine: from the heat transfer prediction to the thermal field evaluation. In: *SAE technical papers*, SAE International; 2017. https://doi.org/10.4271/2017-01-2196.
[51] d'Adamo A, Iacovano C, Fontanesi S. Large-Eddy simulation of lean and ultra-lean combustion using advanced ignition modelling in a transparent combustion chamber engine. Appl Energy 2020;280(Dec). https://doi.org/10.1016/j.apenergy.2020.115949.
[52] D'Adamo A, Breda S, Cantore G. Large-eddy simulation of cycle-resolved knock in a turbocharged SI engine. In: Energy procedia. Elsevier Ltd; 2015. p. 45–50. https://doi.org/10.1016/j.egypro.2015.11.881.
[53] Lee M, Hall M, Ezekoye O, Matthews R. Voltage, and energy deposition characteristics of spark ignition systems. SAE technical papers. Apr. 2005. https://doi.org/10.4271/2005-01-0231.
[54] Huang S, Li T, Ma P, Xie S, Zhang Z, Chen R. Quantitative evaluation of the breakdown process of spark discharge for spark-ignition engines. J Phys D Appl Phys 2020;53(4):045501. https://doi.org/10.1088/1361-6463/ab56da.
[55] Stevens CR. Energy storage and the criteria for proper ignition in the internal combustion engine. IEEE Trans Ind Electron Control Instrum 1965;IECI-12(1):8–13. https://doi.org/10.1109/TIECI.1965.229542.
[56] Herweg R, Maly RR. A fundamental model for flame kernel formation in S. I. Engines. SAE Trans 1992;101:1947–76 [Online]. Available: http://www.jstor.org/stable/44611342.
[57] Trelles JP, Heberlein JVR, Pfender E. Non-equilibrium modelling of arc plasma torches. J Phys D Appl Phys Oct. 2007;40(19):5937–52. https://doi.org/10.1088/0022-3727/40/19/024.
[58] Trelles JP, Chazelas C, Vardelle A, Heberlein JVR. Arc plasma torch modeling. J Therm Spray Technol Dec. 2009;18(5–6):728–52. https://doi.org/10.1007/s11666-009-9342-1.
[59] Haidar J. Non-equilibrium modelling of transferred arcs. J Phys D Appl Phys 1999;32:263–72.
[60] Gleizes A, Gonzalez JJ, Freton P. Thermal plasma modelling. J Phys D Appl Phys May 2005;38(9). https://doi.org/10.1088/0022-3727/38/9/R01.
[61] Lucchini T, et al. A comprehensive model to predict the initial stage of combustion in SI engines. In: *SAE technical papers*, SAE International; Apr. 2013. https://doi.org/10.4271/2013-01-1087.
[62] Willems H, Sierens R. Modeling the initial growth of the plasma and flame kernel in SI engines. J Eng Gas Turbines Power Apr. 2003;125(2):479–84. https://doi.org/10.1115/1.1501912.
[63] Herweg R, Maly RR. A fundamental model for flame kernel formation in S. I. Engines. JOURNAL OF ENGINES Oct. 1992. https://doi.org/10.4271/922243.
[64] Colin O, Truffin K. A spark ignition model for large eddy simulation based on an FSD transport equation (ISSIM-LES). Proc Combust Inst 2011;33(2):3097–104. https://doi.org/10.1016/j.proci.2010.07.023.
[65] Adelman HG. A time dependent theory of spark ignition. Symposium (International) on Combustion 1981;18(1):1333–42. https://doi.org/10.1016/S0082-0784(81)80137-3.
[66] Siemens PLM. DARS v2020.1 Manual - book 2. 2020.
[67] Konnov AA. Refinement of the kinetic mechanism of hydrogen combustion. Adv Chem Phys 2004;23:5–18.
[68] Siemens PLM. STARCD v4.34 manual - methodology. 2020.
[69] Peters N. Turbulent combustion. Cambridge University Press 2000;12(11). https://doi.org/10.1017/CBO9780511612701.
[70] Matalon M. The Darrieus-Landau instability of premixed flames. Fluid Dyn Res Aug. 2018;50(5). https://doi.org/10.1088/1873-7005/aab510.
[71] Millo F, et al. Synergetic application of Zero-, One-, and three-dimensional computational fluid dynamics approaches for hydrogen-fuelled spark ignition engine simulation. SAE Int J Engines Dec. 2021;15(4). https://doi.org/10.4271/03-15-04-0030. 03-15-04–0030.
[72] Piano A, et al. Experimental and numerical investigation of abnormal combustion phenomena in high-performance hydrogen direct-injection engine operated in stochiometric conditions. Int J Engine Res Dec. 2024. https://doi.org/10.1177/14680874241302562.
[73] Liu J, Liu Z. In-cylinder thermochemical fuel reforming for high efficiency in ammonia spark-ignited engines through hydrogen generation from fuel-rich operations. Int J Hydrogen Energy Feb. 2024;54:837–48. https://doi.org/10.1016/j.ijhydene.2023.08.146.
[74] Maio G, et al. Experimental and numerical investigation of a direct injection spark ignition hydrogen engine for heavy-duty applications. Int J Hydrogen Energy Aug. 2022;47(67):29069–84. https://doi.org/10.1016/J.IJHYDENE.2022.06.184.
[75] Bray KNC. In: Libby PA, Williams FA, editors. Topics in applied physics. Springer Verlag; 1980.
[76] Peters N. Twenty-First symposium (International) on combustion. The Combustion Institute; 1988.
[77] Aspden AJ, Day MS, Bell JB. Characterisation of low Lewis number flames. Proc Combust Inst 2011;33(1):1463–71. https://doi.org/10.1016/j.proci.2010.05.090.
[78] Heywood JB. Internal combustion engines fundamentals. 1988. New York.
[79] Pope SB. Turbulent flows. Cambridge: Cambridge University Press; 2000.
[80] Ramalho Leite C, Brequigny P, Borée J, Foucher F. Early flame development characterisation of ultra-lean hydrogen–air flames in an optical spark-ignition engine. Proc Combust Inst 2024;40(1–4):105260. https://doi.org/10.1016/j.proci.2024.105260.